Article

Lithiophilic Nickel Phosphide Modifying Carbon Nanofibers for a Highly Reversible Lithium-Metal Anode

Cuimei Fu, Wangcong Xu, Chengzhou Tao, Lina Wang,* and Tianxi Liu*

Read Online

ACCESS | Metrics & More | Article Recommendations | Supporting Information

ABSTRACT: A lithium (Li)-metal battery with high energy density is the most promising system for the next-generation battery. However, detrimental Li dendrite growth induced by uneven Li deposition causes inferior Coulombic efficiency (CE) and infinite volumetric expansion of Li-metal anodes. Herein, a flexible carbon nanofiber membrane modified by nickel phosphide ($Ni_2P@CNF$) is proposed as an effective 3D framework to guide Li deposition behaviors. Even and dense deposition of Li is observed via *ex situ/in situ* morphological observations, ascribed to the homogeneous Li nucleation on the lithiophilic Ni_2P crystalline grains. The efficient utilization of Li is achieved benefiting from the synergistic reversible conversion reactions between Li and Ni_2P and plating/stripping of Li. Moreover, the fibrous networks of $Ni_2P@CNF$ retain structural stability upon prolonged cycling. Thus, an average CE of 97.6% at 5 mA cm^{-2} is available. And an extended lifespan of 2000 h at 0.5 mA cm^{-2} for a symmetrical cell of $Ni_2P@CNF@Li$ and 1000 cycles at 5 C (1 C = 170 mA g^{-1}) for a Li||LiFePO$_4$ cell are attained, revealing the great potential of a practical Li-metal anode.

KEYWORDS: Ni_2P, nanofibers, lithium deposit behaviors, lithium metal anodes, in situ observations
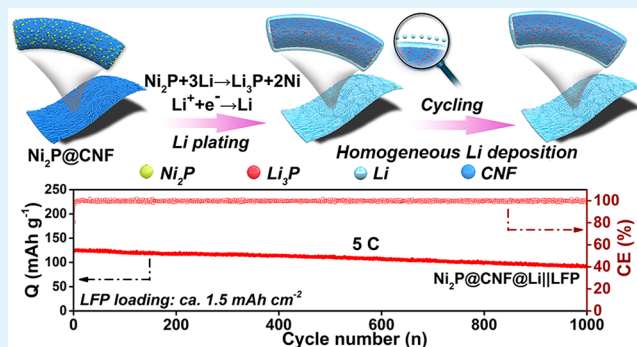
1. INTRODUCTION

To satisfy the demands for high-energy-density technology, it becomes more and more imperative to explore new tactics beyond lithium (Li)-ion chemistry.[1,2] One plausible approach is to employ Li-metal batteries with Li-metal anodes, which possess incomparable merits of the most electronegative potential (−3.04 V vs SHE), ultrahigh theoretical capacity (3860 mAh g^{-1}), and the lightest density (0.534 g cm^{-3}).[3−8] However, inferior Coulombic efficiency (CE) and cyclic stability as well as safety hazards have severely impeded the practical application of Li-metal anodes.[3,4,9] The infinite volumetric expansion of "hostless" Li and inhomogeneous ion/electron distribution on the surface cause the needle-like Li dendrite evolution,[9−12] which not only can induce low utilization of Li but also trigger an internal short circuit of batteries.[3,4,12]

Up to now, substantial efforts have been devoted to resolve the aforementioned obstacles. Surface engineering of Li metal by an artificial coating layer (e.g., Li$^+$ conductive alloy as well as LiF-containing and solution-based reactions, etc.) or *in situ* modification by additives in an electrolyte (e.g., fluoroethylene carbonate, acetonitrile, LiAsF$_6$, etc.) are proposed to adjust Li deposition.[13−20] Insufficient Li$^+$ migration within the fragile surface layer causes the growth of Li dendrites under high current densities.[21,22] Alternatively, rational design of a three-dimensional (3D) conductive framework, such as 3D copper,

nickel foam, and graphene, etc., is capable of mitigating the volumetric expansion of "hostless" Li.[23−26] Also, the 3D conductive hosts can enhance the charge transfer and homogenize the electrical field distribution to obtain a relatively steady state of Li$^+$ concentration.[27,28] However, the lithiophobic nature of the frameworks with a large nucleation barrier prevents uniform Li nucleation and deposition.[29,30] Heterogeneous Li$^+$ flux would tend to gather on the surface to accept the electrons easily, leading to the risk of uncontrollable Li dendrite formation. To improve the Li affinity, lithiophilic Li nucleation sites have been incorporated into the frameworks,[31−33] for example, lithiophilic metal (silver nanowire aerogel, Li−Al alloy, porous Cu and Li−Mg alloy, etc.)[34−38] and metal oxides or sulfides (SiO$_x$, ZnO layer, and Cu$_2$S nanowires, etc.).[39−42] Nevertheless, structural expansion and pulverization due to an alloy reaction[43] or increasing polarization by isolated Li$_2$O or Li$_2$S derived from lithiation can cause uneven Li electroplating during the repeated cycling under a high rate.[44,45] Recently, metallic phosphides were
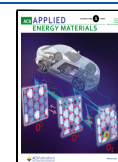
reported as lithiophilic seeds for Li nucleation owing to their good conductivity, strong reaction with Li, and the high Li^+ conductivity of Li_3P from the lithiation reaction.[46−48] Despite these ideal strategies, a simple phosphorization method to obtain well-distributed lithiophilic metallic phosphides on a flexible host with effective Li storage is still imperatively demanded.

Herein, a lithiophilic Ni_2P-modified carbon nanofiber ($Ni_2P@CNF$) host is proposed to guide the Li deposition behavior and accommodate the volumetric expansion for prolonged cycling processes. Ni_2P with a lithiophilic property also exhibits a reversible conversion reaction with Li, providing abundant Li nucleation sites. Electrochemical and spectroscopic characterizations along with *ex situ/in situ* morphological observations illuminate the homogeneous and compact Li deposits on $Ni_2P@CNF$. On account of synergistic structural stability and lithiophilic chemical composition, the $Ni_2P@CNF@Li$ anode can work stably over 2000 h at 0.5 mA cm^{-2} for 1 mAh cm^{-2}. And average CEs of 98.6 and 97.6% for 400 and 200 cycles under 1 and 5 mA cm^{-2} with limited 1 mAh cm^{-2} Li are achieved, respectively. Moreover, $Ni_2P@CNF@Li$ coupled with a high-loading $LiFePO_4$ cathode (10 mg cm^{-2}, 1.5 mAh cm^{-2}) delivers a reversible capacity exceeding 90 mAh g^{-1} with a CE of ~99.1% for 1000 cycles at 5 C, manifesting its available practical applications for lithium-metal batteries.

2. EXPERIMENTAL SECTION

2.1. Materials. Nickel acetate tetrahydrate ($C_4H_6NiO_4·4H_2O$, 98%), phosphorus oxide (P_2O_5, 98%), and *N,N*-dimethylformamide (DMF, C_3H_7NO, 99.5%) were purchased from Sinopharm Chemical Reagent. Polyacrylonitrile (PAN, average M_w 150 000) was provided by Sigma-Aldrich. All chemical reagents in this paper were used without further treatments.

2.2. Fabrication of $Ni_2P@CNF$. $Ni_2P@CNF$ was synthesized via a moderate electrospinning process and a succeeding heat treatment. Typically, DMF (10 g) containing $C_4H_6NiO_4·4H_2O$ (0.39 g) and P_2O_5 (0.2 g) solution was obtained under magnetic stirring. Subsequently, PAN (1 g) was added into the above mixture with sustained stirring overnight to form a homogeneous solution. Next, the above solution was filled into a 10 mL syringe for electrospinning (ET2531, Beijing Ucalery Technology) under a high voltage (15−20 kV) with a distance of 16−20 cm. Finally, the obtained membrane was calcinated under 800 °C for 3 h (5 °C min^{-1}, N_2 flow) to perform the carbonization and reducing reaction processes, donated as $Ni_2P@CNF$. A Ni_2P-free CNF was fabricated under identical procedures with absent $C_4H_6NiO_4·4H_2O$ and P_2O_5. The average loading of $Ni_2P@CNF$ and CNF electrodes was controlled as ~3.0 mg cm^{-2}.

2.3. Electrochemical Measurements. The battery performance of the as-obtained $Ni_2P@CNF$ and CNF was evaluated by assembling CR2025 coin-type cells. Celgard 2325 film (thickness: 25 μm) was employed as the separator for all kinds of batteries in this work. For the ether electrolyte, 1 M bis(triuoromethane)sulfonimide lithium salt (LiTFSI) dissolved in 1,3-dioxolane (DOL)/1,2-dimethoxyethane (DME) (vt%, 1:1) with 0.2 M lithium nitrate ($LiNO_3$) additive was served. The carbonate electrolyte was 1.0 M $LiPF_6$ dissolved in ethylene carbonate (EC)/dimethyl carbonate (DMC)/diethyl carbonate (DEC) (1:1:1, v/v/v). The amount of the electrolyte is controlled as 50 μL. To deposit Li on the substrate, the counter electrode of Li foil was directly used. The electrochemical performance was recorded on a Land battery system tester. For CEs of the $Ni_2P@CNF$, the batteries were activated under 0.5 mA at 0.1−1 V (vs Li/Li^+) for three cycles for stabilizing the SEI layer. Subsequently, the measurement was implemented by discharged 1 mAh cm^{-2} Li and stripped to 1 V.

Symmetrical cells with two sheets of identical electrodes were employed to measure the Li depositing/stripping behaviors of $Ni_2P@$

CNF@Li. Li (10 mAh cm^{-2}) was pre-electrodeposited onto the substrates under 0.5 mA cm^{-2}. Li||Li symmetrical cells were assembled for reference. Cu@Li and CNF@Li symmetrical cells were tested under the same conditions as a control. Electrochemical impedance spectroscopy (EIS) measurements were performed on a CHI660E workstation under an amplitude of 5 mV and open-circuit potential with a frequency of 0.01 Hz−100 kHz.

To evaluate the feasibility of the $Ni_2P@CNF@Li$, $LiFePO_4$ (LFP) was served as a cathode. LiTFSI (1 M) dissolved in DOL/DME (vt%, 1:1) with a 0.2 M $LiNO_3$ additive was served as the electrolyte. Typically, $Ni_2P@CNF$ was pre-electrodeposited with 10 mAh cm^{-2} of Li. Here, $LiFePO_4$ ($LiFePO_4$:carbon black:polyvinylidene difluoride = 90:5:5) with an areal capacity of ~1.5 mAh cm^{-2} (ca. 10 mg cm^{-2}) on aluminum foil (*d* = 12 mm) was coupled with $Ni_2P@CNF@Li$. CNF@Li||LFP was assembled under identical procedures as a control. For comparison, Li foil and LFP electrodes were directly assembled. And voltage windows between 2 to 4 V vs Li/Li^+ were all configured.

3. RESULTS AND DISCUSSION

3.1. Fabrication and Characterizations of $Ni_2P@CNF$. The synthetic route of $Ni_2P@CNF$ involved a versatile electrospinning and succeeding carbothermic reduction. The as-spun films were obtained from DMF homogeneous solutions containing PAN, $C_4H_6NiO_4·4H_2O$, and P_2O_5. Subsequently, the dried precursor membrane was calcined at 800 °C under N_2 flow for 3 h. Ni_2P was formed *in situ* during the heat reduction treatment. PAN acts as the electrospinning substrate with desirable rheological properties in the synthetic process. Moreover, CO and H_2 released from the pyrolysis of PAN create a strong reducing atmosphere (Figure S1). As schematically described in Figure 1a, a Ni_2P-modified CNF skeleton guides the Li deposition to nucleate and grow uniformly compared with the unmodified CNF, which presents a promise to render a nondendritic lithium-metal anode.
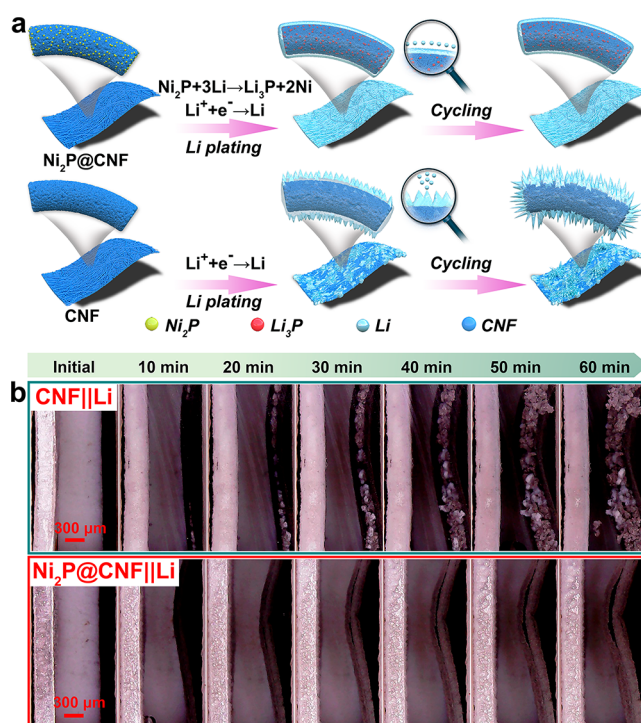

Figure 1. (a) Schematic illustrations of Li deposition behavior on $Ni_2P@CNF$ compared with CNF. (b) The *in situ* optical observation of Li deposition behavior on CNF or $Ni_2P@CNF$ with a counter electrode of Li foil (the left side).

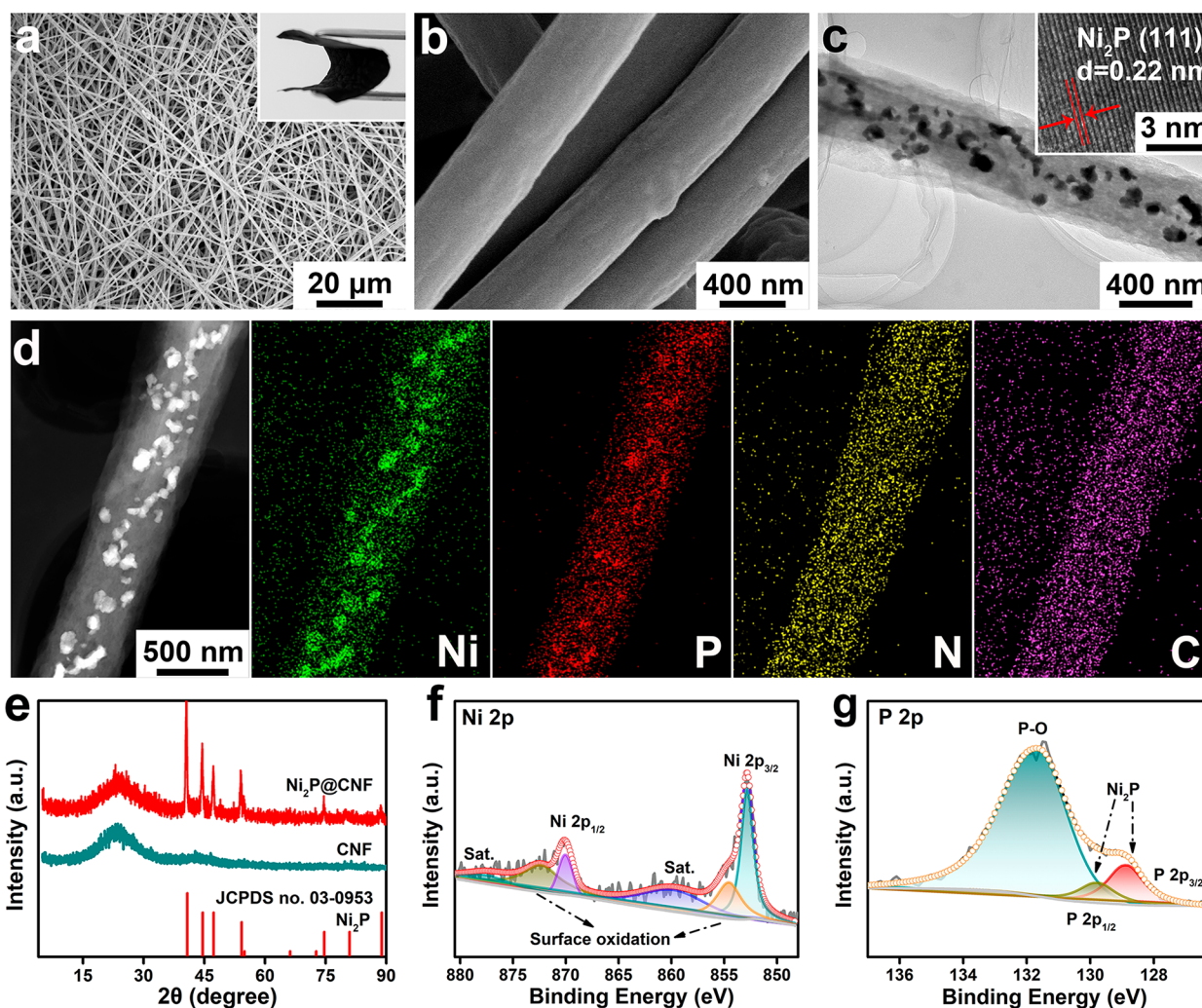**Figure 2.** Characterizations of $Ni_2P@CNF$. (a,b) SEM images of a flexible $Ni_2P@CNF$ membrane. The inset in (a) is a digital photo. (c) TEM images and lattice fringes of Ni_2P (111). (d) Scanning transmission electron microscopy images of $Ni_2P@CNF$. (e) XRD patterns and XPS of (f) Ni 2p and (g) P 2p spectra.

Intuitively, the selected optical microscopy images for *operando* observation were illustrated in Figure 1b to estimate the Li dendrite inhibition of $Ni_2P@CNF$. The visualized cells of $Ni_2P@CNF$ and CNF as the working electrode were assembled, with the Li foil as the counter electrode. Noticeable Li protuberances emerge at the edges of CNF and arouse the aggregation of Li nuclei with inhomogeneous Li plating. High dendrite and bulky Li deposition is generated quickly. In comparison, no sign of branched-like Li is observable for $Ni_2P@CNF$, with compact and uniform Li deposition. A smaller thickness of the Li deposition layer is observed than CNF, signifying the $Ni_2P@CNF$ is capable to uniformize deposition of Li^+ and suppress the formation of Li dendrites.

Scanning electron microscopy (SEM) and transmission electron microscopy (TEM) were employed to disclose the morphology microstructure of the $Ni_2P@CNF$. The precursor of $Ni_2P@CNF$ exhibits a nanofibrous-network structure (Figure S2), with a uniform diameter of approximately 700 nm. The porous surface of $Ni_2P@CNF$ nanofibrous network is maintained during the pyrolysis process (Figure 2a), with a diameter of ~500 nm (Figure 2b). And the as-synthesized $Ni_2P@CNF$ texture is flexible (the inset in Figure 2a), which can be effortlessly tailored into fracture-free and freestanding

electrodes. Similar morphology is observed in CNF without Ni_2P incorporation (Figure S3). TEM images demonstrate that the Ni_2P is uniformly distributed over the nanofiber (Figure 2c). The lattice fringes with a *d*-spacing of 0.22 nm can be obviously identified in a high-resolution TEM image (the inset in Figure 2c), corresponding to the hexagonal Ni_2P (111) plane (JCPDS no. 03−0953). The elemental mapping analysis shows uniform distributions of C and N elements throughout the nanofiber (Figure 2d). The mapping images of Ni and P exhibit obvious accumulation, which confirm the fine dispersion of Ni_2P nanoparticles. Correspondingly, the special surface area of $Ni_2P@CNF$ is determined as 64.4 m^2 g^{-1} by the Brunauer−Emmett−Teller method (Figure S4a), which is higher than that of CNF (15.0 m^2 g^{-1}). The mesopores and macropores in the $Ni_2P@CNF$ porous structure are derived from the gas release and internal crystallization of Ni_2P during the calcination process (Figure S4b).

The phase structure of $Ni_2P@CNF$ was investigated by X-ray diffraction (XRD) measurements (Figure 2e), which verify the formation of the high crystallinity of the hexagonal Ni_2P phase (JCPDS no. 03−0953). The lattice plane of carbon (JCPDS no. 26−1079) is appearing at ~26° with a broad peak, derived from graphitization of PAN during pyrolysis treatment.
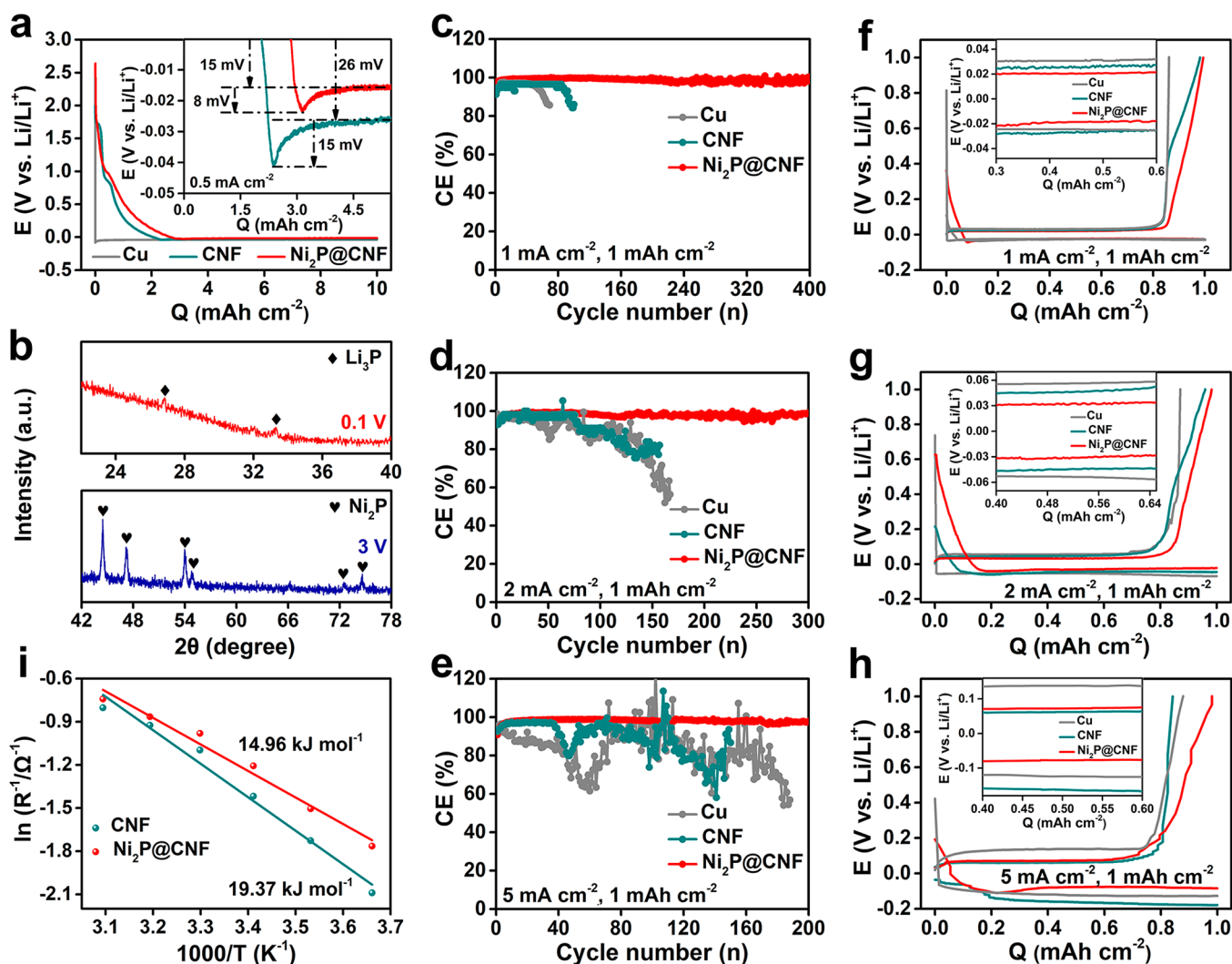
Figure 3. Electrochemical characteristics of Ni$_2$P@CNF. (a) Voltage−capacity profiles at 0.5 mA cm^{-2}. (b) XRD patterns of initial cycles under 0.1 and 3 V (Li full stripped) at 0.5 mA cm^{-2}. CEs performance at (c) 1, (d) 2, and (e) 5 mA cm^{-2}, and (f–h) the corresponding voltage profiles with limited 1 mAh cm^{-2} Li. (i) Arrhenius plots.

Raman spectroscopy was implemented to analyze degree of graphitization of Ni$_2$P@CNF (Figure S5). And the intensity ratio of the D band (~1350 cm^{-1}, diamond-like) to the G band (~1590 cm^{-1}, graphite-like) (I_D/I_G) is ~1.005,[49,50] higher than that of CNF (I_D/I_G = 0.955), suggesting a relatively high disorder degree of amorphous carbon and abundant defects in Ni$_2$P@CNF. The C content of 45 and 83 wt % in Ni$_2$P@CNF and CNF was determined by elemental analysis (Table S1), while the respective N content is 7 and 12 wt %, respectively. The content of Ni$_2$P was confirmed by TGA under air atmosphere (Figure S6a). After annealing, Ni$_2$P is oxidized to NiO, Ni$_2$P$_2$O$_7$, and Ni$_3$(PO$_4$)$_2$ (Figure S6b). And the content of Ni$_2$P is calculated to be ~41 wt %.

X-ray photoelectron spectroscopy (XPS) characterizations were implemented to further investigate the surface elemental species and chemical valence state of Ni$_2$P@CNF. Ni, P, N, and C have been observed in the survey XPS spectrum (Figure S7a). As displayed in Figure 2f, Ni core level peaks situated at 852.8 and 870.1 eV are associated with Ni 2p$_{3/2}$ and 2p$_{1/2}$ of nickel phosphides, respectively.[51−53] A doublet located at 854.6 and 872.5 eV is attributed to the inevitable surface trace oxidation of Ni$_2$P in air.[54] And the peaks at 860.5 and 878.0 eV

correspond to satellite peaks (abbreviated as "sat.").[51,53] In the P 2p spectrum (Figure 2g), the doublet at 128.9 and 129.8 eV is assigned to the P 2p$_{3/2}$ and 2p$_{1/2}$ of Ni$_2$P,[55] respectively, whereas a peak around 131.9 eV is related to the oxidized P species.[56] The deconvolution of the N 1s spectrum (Figure S7b) at 403.0, 400.2, and 397.6 eV is attributed to oxidized N, pyrrolic N, and pyridinic N, respectively.[57,58] And the C 1s spectrum has been fitted by corresponding two peaks at 284.8 and 286.1 eV (Figure S7c), which are ascribed to graphitic C and C−N, respectively.[59,60]

3.2. Li Deposition Behaviors of Ni$_2$P@CNF. The lithiophilicity and deposition behaviors of Ni$_2$P@CNF were investigated, and pure Li was served as the counter electrode under 0.5 mA cm^{-2} for 10 mAh cm^{-2} Li (Figure 3a). Before Li plating, a weak voltage plateau at ~1.0 V is observed, which implies the adsorption reaction of active Li$^+$ into porous nanofibers.[61] The insertion reaction of Li$^+$ into graphitic carbon layers appears below 0.5 V. The general sloping voltage plot in Ni$_2$P@CNF is attributed to the pseudocapacitive dominant Li$^+$ storage for the conversion reaction of nanosized Ni$_2$P with Li (Ni$_2$P + 3Li ↔ Li$_3$P + 2Ni). A pseudocapacitive charge storage mechanism endows high charge/discharge rates
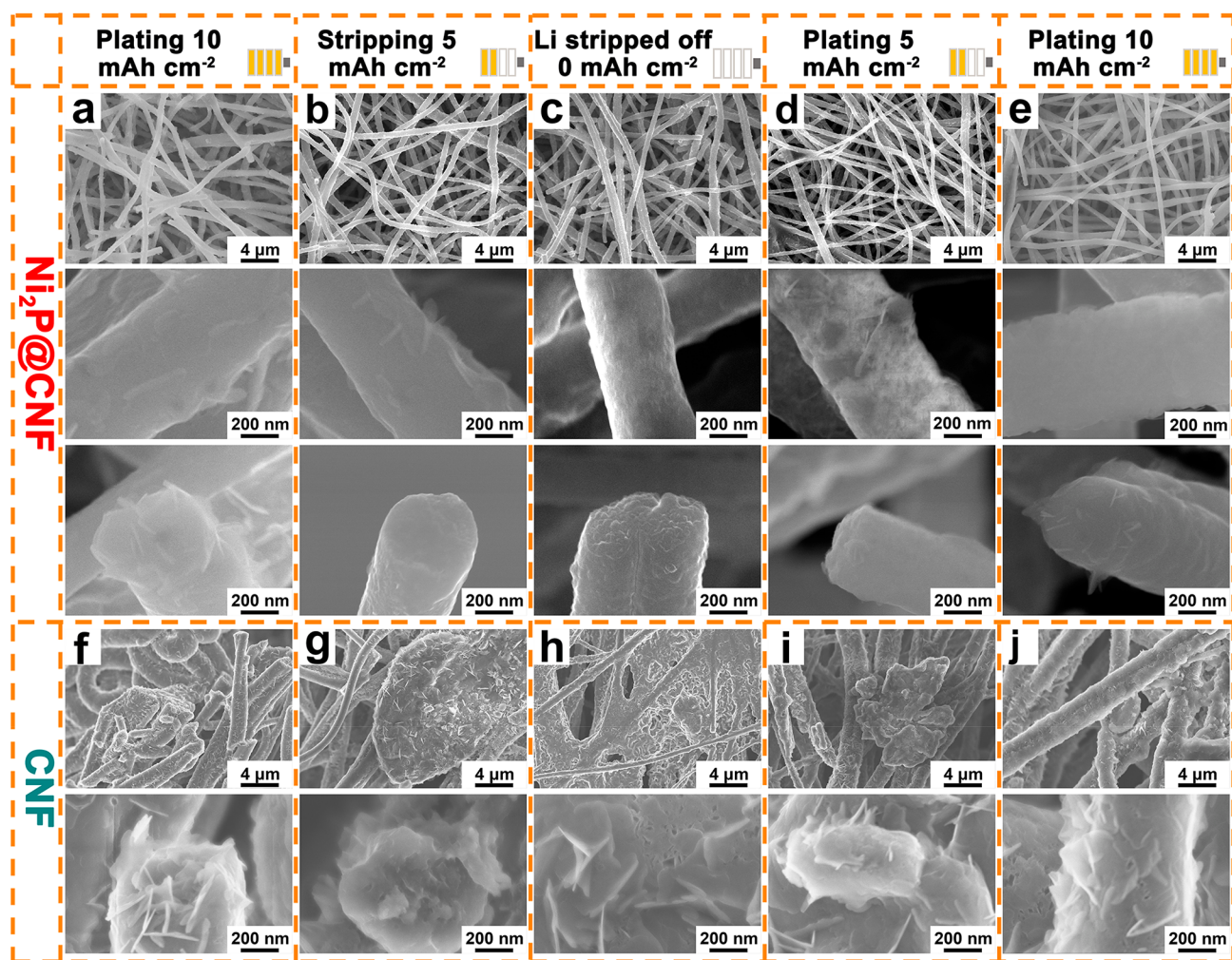
Figure 4. SEM morphological evolution of (a−e) Ni₂P@CNF and (f−j) CNF during Li plating/stripping at 0.5 mA cm⁻².

of surface reactions of Ni₂P.[62,63] The formation of nucleation seeds induced by the lithiation of Ni₂P is accomplished during the initial discharging process. Generally, the charge distribution and lithiophilicity of the skeleton hold dominance over the Li nucleation overpotential, which is determined by the gap from the dip to the subsequent voltage plateau. Compared with that of CNF (15 mV) and Cu foil (42 mV, Figure S8), the Li nucleation overpotential of Ni₂P@CNF is only 8 mV, implying the favorable affinity of Ni₂P@CNF to Li. In contrast to that of CNF (26 mV) and Cu foil (39 mV), the growth overpotential for Ni₂P@CNF is only 15 mV, indicating the homogeneous charge distribution and feasible Li nucleus growth on Ni₂P@CNF. Furthermore, *ex situ* XRD measurements were performed to verify the resultants of initial discharging to 0.1 V and Li fully stripped to 3 V (Figure 3b). Li₃P and Ni₂P (JCPDS no. 74−1160 and 03−0953) for 0.1 and 3 V are identified, respectively, which validate the reversible conversion reaction of Ni₂P with Li. During the lithiation process, the lithiophilic Ni₂P and the formation of Li₃P improve the affinity with Li and provide more nucleation sites for Li depositing into the Ni₂P@CNF skeleton. Meanwhile, the reverse reaction guides uniform Li stripping from the whole skeleton and compensates irreversible Li consumption, further suppressing the formation of dendritic Li.

The Coulombic efficiency (CE) implies the reversibility of Li-repeated depositing and stripping of the Ni₂P@CNF,

determined from the ratio of the Li stripped capacity to a limited Li deposition of 1 mAh cm⁻². The CE of Ni₂P@CNF electrode reaches 99.0% at a moderate 1 mA cm⁻² (Figure 3c) and eventually maintains 98.6% over 400 cycles. Upon increasing to 2 mA cm⁻², the CE is still stabilized at 98.4% even after 300 cycles (Figure 3d). A CE of 97.6% is achieved at a better 5 mA cm⁻² and remains stable over 200 cycles (Figure 3e), attributed to the uniform Li electrodeposition guided by the reversible conversion reaction of lithiophilic Ni₂P. In contrast, the pristine Cu electrode presents much worse CE performance of 85% at 1 mA cm⁻² for 65 cycles and 60% for 63 cycles at 5 mA cm⁻². Meanwhile, CNF delivers inferior CE performance of 84.2% (1 mA cm⁻²) and 58% (5 mA cm⁻²) for 100 and 140 cycles, respectively. The plating/stripping overpotential also significantly embodies the interfacial resistance during cycling (Figure 3f−h). Notably, the plating/stripping overpotential of Cu and CNF is obviously higher than Ni₂P@CNF under the same current density. And the overpotential of Cu and CNF drastically enlarges as the current density increases, while Ni₂P@CNF fluctuates slightly, demonstrating a fast Li⁺ diffusion kinetics of the lithiophilic Ni₂P-enhanced CNF. Moreover, EIS measurements of the temperature-dependent interfacial resistance were implemented to probe the Arrhenius activation energy of Ni₂P@CNF ranging within 273 to 323 K (Figure S9). And the corresponding Arrhenius plots are obtained complying with
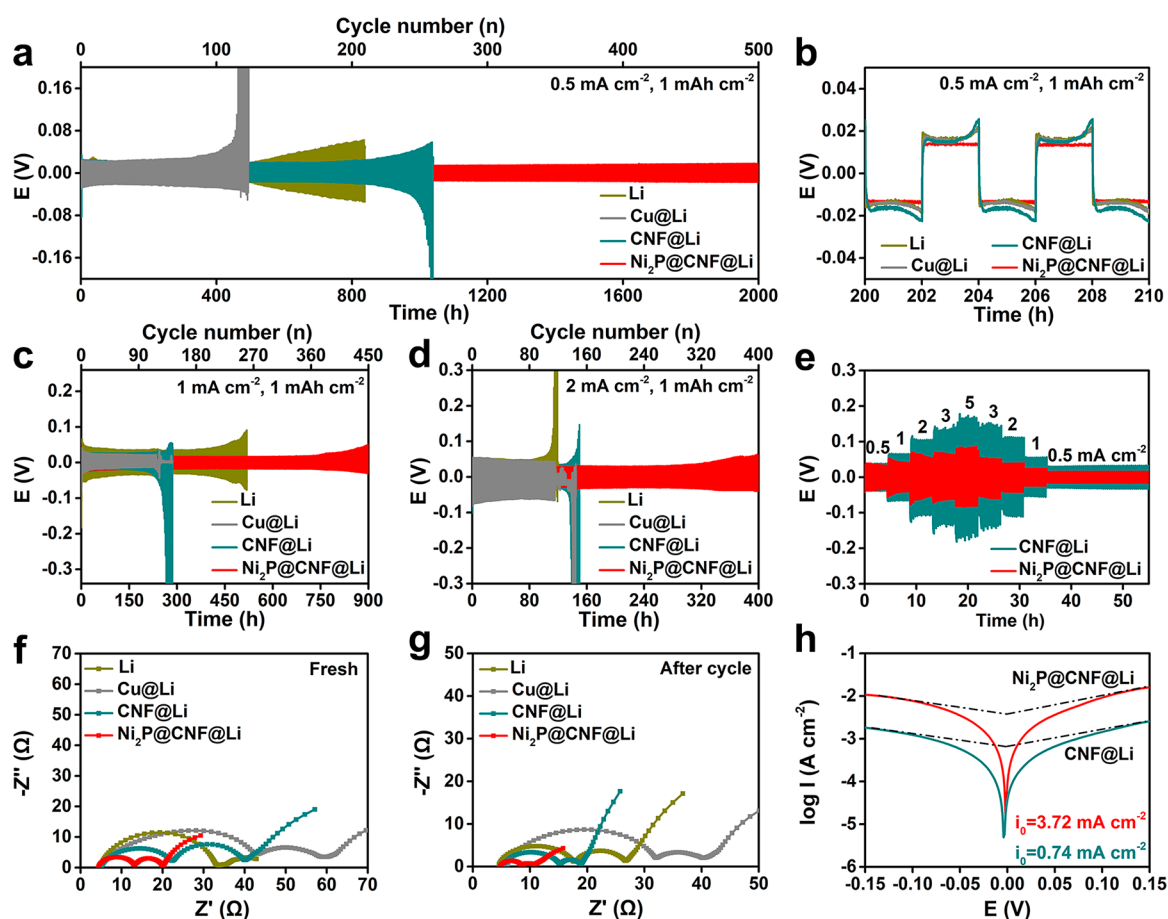
Figure 5. Electrochemical performances of symmetrical cells for $Ni_2P@CNF@Li$. (a) The cycling stability and (b) corresponding voltage curves at 0.5 mA cm^{-2}. Galvanostatic cycling performance at (c) 1 and (d) 2 mA cm^{-2} for 1 mAh cm^{-2}. (e) Rate performance. EIS plots for (f) fresh symmetrical cells and (g) after 100 cycles at 1 mA cm^{-2}. (h) Tafel plots.

the law of Arrhenius (Figure 3i).[38,64] The activation energy of $Ni_2P@CNF$ and CNF was determined to be 14.96 and 19.37 kJ mol^{-1}, respectively, indicating an express mass transfer of $Ni_2P@CNF$ substrate.

The Li deposition behavior on the $Ni_2P@CNF$ is illustrated in Figure 4 at 0.5 mA cm^{-2} for 10 mAh cm^{-2}. The morphological evolution of the $Ni_2P@CNF@Li$ anode at different deposition states upon cycling was elucidated by SEM. The integrity of the 3D nanofibrous network of $Ni_2P@CNF$ is substantially maintained during the overall Li deposition and stripping steps. The surface of the pristine $Ni_2P@CNF$ is relatively smooth, with a diameter of 500 nm (Figure 2b). Along with the 10 mAh cm^{-2} Li plating, the diameter of the nanofiber varies to 650 nm, and Li is completely deposited on the $Ni_2P@CNF$ individual nanofibers (Figure 4a). Distinguished from the pristine nanofibers, the plated nanofibers are covered by nanoflakes. The affinity of Ni_2P and the lithiation reaction of Ni_2P enable the uniform Li deposition on $Ni_2P@CNF$. For the succeeding Li stripping procedure, nanofibrous $Ni_2P@CNF$ is modulated following a gradually decreasing diameter of the individual nanofiber (Figure 4b). And the deposition of Li nanoflakes almost disappears after Li is stripped thoroughly (Figure 4c). Obviously, no residual dendritic bulk Li deposits emerge on the $Ni_2P@CNF$. In the subsequent plating process for 5 (Figure 4d) and 10 mAh cm^{-2} Li (Figure 4e), a compact and dense Li depositing is retained with conformal Li deposits over

the individual fibers. The nanoflake nucleation, growth, and decomposition of the Li nucleus seed are repeated upon cycling. Whereas, sparse Li is deposited on the CNF individual nanofibers, and the porous morphology of bulky Li preferentially grows, enclosing edges of the nanofibers (Figure 4f) as well as rendering the growth of dendrites and a large Li^+ diffusion resistance. In the following Li stripping/plating process, it could be observed that lots of dendritic bulk Li unevenly deposits on the surface of CNF (Figure 4g–j). Moreover, the cross-sectional SEM images demonstrate the perpendicular thickness of $Ni_2P@CNF@Li$ (Figure S10). A volume expansion of ~19% of $Ni_2P@CNF$ is maintained, much lower than that of CNF (68%). This result indicates $Ni_2P@CNF$ is qualified to accommodate Li and handle the volume changes during repeat cycling. The strong Li affinity of Ni_2P and unobstructed mass transfer channels of $Ni_2P@CNF$ empower the absence of dendritic Li on $Ni_2P@CNF$. And the Li_3P derived from the lithiation reaction on the nanofibers serves as the mass transfer centers owing to its fast ionic conducting characteristic.

The galvanostatic cycling measurements of symmetrical cells were investigated to estimate the stability of stripping/depositing behaviors of $Ni_2P@CNF@Li$ anodes at 0.5–2 mA cm^{-2} with a fixed capacity of 1 mAh cm^{-2} (Figure 5). All electrodes were pre-electrodeposited with 10 mAh cm^{-2} Li under 0.5 mA cm^{-2}. $Ni_2P@CNF@Li$ exhibits a long-term cycling stability for 2000 h (500 cycles) at 0.5 mA cm^{-2}
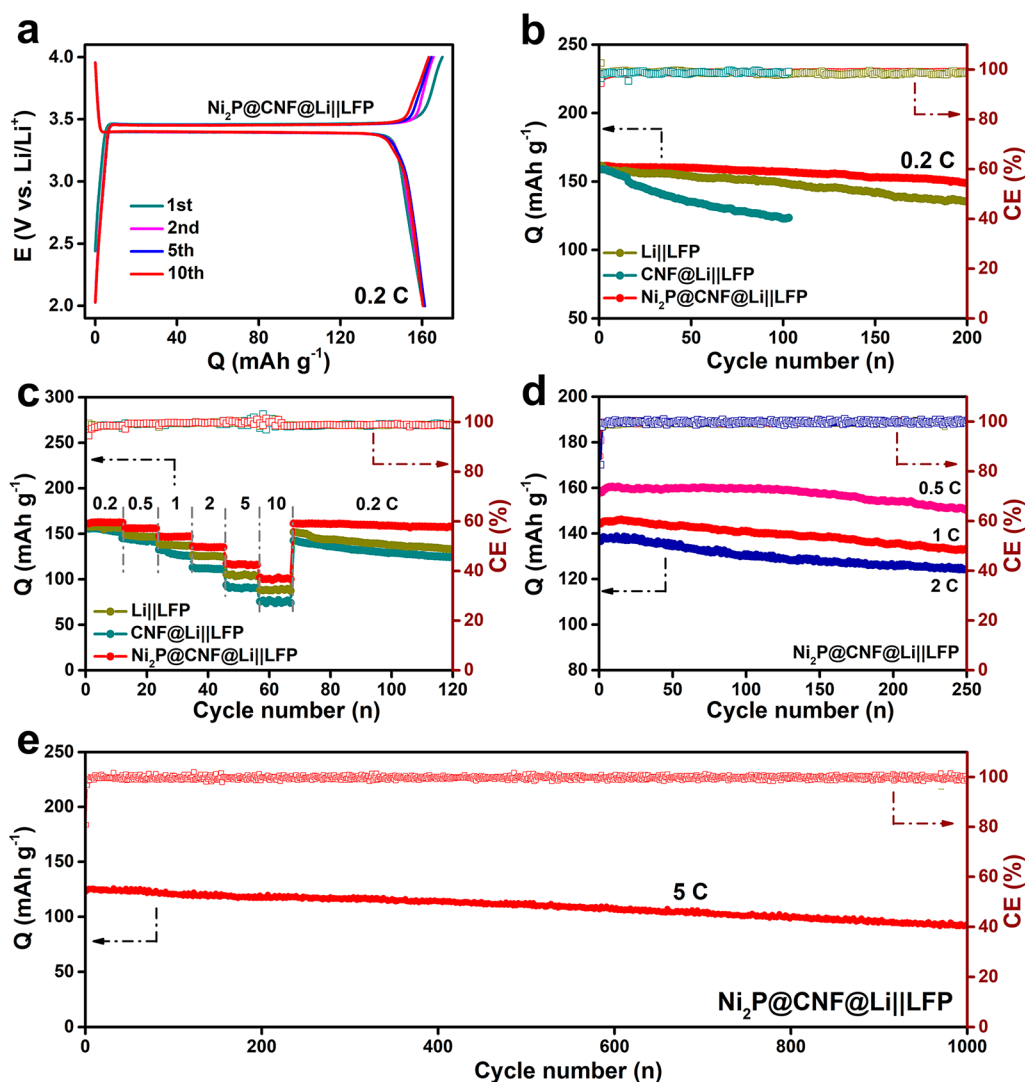
Figure 6. Electrochemical performances of Ni$_2$P@CNF with LiFePO$_4$ cathodes. (a) Voltage−capacity profiles of Ni$_2$P@CNF@Li∥LFP at 0.2 C (1 C = 170 mA g^{-1}). (b) Cycling performances at 0.2 C and (c) rate capability. Long-term cycling performances of Ni$_2$P@CNF@Li∥LFP at various current densities of (d) 0.5, 1, 2, and (e) 5 C.

(Figure 5a), with a voltage hysteresis of 13 mV (Figure 5b). The cells with Li foils, Cu@Li, and CNF@Li exhibit relatively large voltage polarization, which almost can be attribute to the higher interfacial resistance caused by the dendrite Li growth and the accumulation of thick SEI. Remarkably, as the current density increases to 1 and 2 mA cm^{-2}, the Ni$_2$P@CNF@Li-metal anode delivers stable overpotentials of 18 and 30 mV and maintains stabilities of 900 (450 cycles) and 400 h (400 cycles) (Figure 5c,d), respectively. Meanwhile, Li foils, Cu@Li, and CNF@Li-metal anodes display inferior stability, quickly deteriorated by a dramatic value of voltage polarization, and even short-circuit finally. SEM images after 100 cycles at 1 mA cm^{-2} (1 mAh cm^{-2}) with a thickness of 116 μm further demonstrate the dendrite-free Ni$_2$P@CNF@Li and dense Li deposition during cycling (Figure S11). Moreover, the Ni$_2$P@CNF@Li anode expresses enhanced rate stability upon switching variable current densities (Figure 5e). The cycling performance of Ni$_2$P@CNF@Li for symmetric cells precedes many previous works of the previously reported 3D skeleton Li-metal anode (Table S2). Nyquist plots for fresh symmetrical cells (Figure 5f) and those after 100 cycles (Figure 5g) under 1 mA cm^{-2} elucidate Li$^+$ diffusion and the charge transfer of

Ni$_2$P@CNF@Li. Typically, the first semicircle relates to the SEI resistance, and the second semicircle is associated with charge transfer resistance. A lower charge transfer resistance of Ni$_2$P@CNF@Li for both fresh cells and those after 100 cycles demonstrates the enhanced mass transport to inhibit the formation of Li dendrites, which is in accordance with the stable Li plating/stripping curves in Figure 5c. Considering the small voltage polarization of Ni$_2$P@CNF@Li, the exchange current density (i_0) of Ni$_2$P@CNF@Li was determined from the Tafel slopes by linear sweep voltammetry measurements (Figure 5h) to further reveal the charge transfer kinetics. The i_0 values of Ni$_2$P@CNF@Li and CNF@Li are 3.72 and 0.74 mA cm^{-2}, respectively, indicating that the modified Ni$_2$P@CNF@Li effectively facilitates the kinetics of Li migration and thereby boosts the electrochemical performance. The compatibility of Ni$_2$P@CNF@Li in carbonate electrolytes was also studied using EC/DMC/DEC (1:1:1, v/v/v) with 1 M LiPF$_6$. The Li nucleation and growth overpotential on Ni$_2$P@CNF are 19 and 27 mV at 0.5 mA cm^{-2} (Figure S12a), respectively. A CE of 98.3% is achieved at 1 mA cm^{-2} and maintains 97.9% after 150 cycles (Figure S12b). The corresponding voltage profiles suggest reversible Li plating/stripping with an overpotential of

33 mV (Figure S12c). The symmetrical cells of Ni$_2$P@CNF@Li exhibit stable cycling at 1 mA cm^{-2} over 300 h and at 2 mA cm^{-2} over 140 h (Figure S12d,e), respectively. The inferior CE and cyclic stability of Ni$_2$P@CNF in a carbonate-based electrolyte suggest carbonate solvents are more corrosive than ether toward Li.[65,66]

3.3. Applications of Ni$_2$P@CNF@Li with LiFePO$_4$ Cathodes.
For emphasizing the feasibility of Ni$_2$P@CNF@Li, galvanostatic cycling measurements with LiFePO$_4$ (LFP) cathodes were implemented. The voltage−capacity plots of Ni$_2$P@CNF@Li‖LFP exhibit an obvious plateau of 3.45 V under 0.2 C (1C = 170 mA g^{-1}) (Figure 6a). Additionally, the voltage curves of both oxidation and reduction are well-repetitive from the 1st to 10th cycles, suggesting a good reversibility of Li-metal anodes based on Ni$_2$P@CNF@Li. A specific capacity of 150 mAh g^{-1} after 200 cycles is maintained with a capacity retention of 93% for Ni$_2$P@CNF@Li (Figure 6b). Li‖LFP (135 mAh g^{-1}, 200 cycles) and CNF@Li‖LFP (123 mAh g^{-1}, 100 cycles) possess inferior capacity retentions of 83 and 76%, respectively. The advantage of Ni$_2$P@CNF@Li becomes more obvious in a rate capability measurement (Figure 6c). Ni$_2$P@CNF@Li‖LFP display a capacitiy of 100 mAh g^{-1} at 10 C, 50-fold higher than the initial rate. And reversible capacities of 161 mAh g^{-1} are still retained as resetting to 0.2 C. Benefiting from the uniformized mass transport, the Ni$_2$P@CNF@Li‖LFP cells also exhibit high specific capacities of 151 (0.5 C), 133 (1 C), and 124 (2 C) mAh g^{-1} for 250 cycles (Figure 6d). Notably, the Ni$_2$P@CNF@Li‖LFP offers a capacity of 92 mAh g^{-1} under a better rate of 5 C upon 1000 cycles, delivering an average CE of 99.1% (Figure 6e).

4. CONCLUSIONS

In summary, we have successfully developed a straightforward strategy of a 3D Ni$_2$P@CNF substrate to obtain nondendritic Li growth. The ideal conversion reaction from lithiophilic Ni$_2$P and Li to Li$_3$P not only enhances the Li affinity of the skeleton but also obviously regulates nondendritic Li deposition with enhanced CE via uniformized mass transport and accelerated electrochemical kinetics. Furthermore, the interconnected nanofibrous structure ensures structural stability and further alleviates the huge dimensional volume variations of Li during cycling. The active Li reserved can compensate irreversible Li consumption during cycling owing to the reversible conversion reaction of Ni$_2$P, which prolongs the lifespan of the battery. Additionally, the nondendritic Li deposition on the Ni$_2$P@CNF substrate is disclosed by means of *ex situ/in situ* morphological observations. Therefore, a long lifespan with a stable overpotential over 2000 h at 0.5 mA cm^{-2} is maintained using as-formed Ni$_2$P@CNF@Li anodes. Coupled with a high-loading LFP cathode (ca. 10 mg cm^{-2}), the Ni$_2$P@CNF@Li‖LFP cell exhibits long cycling life over 1000 cycles, with enhanced rate capability (over 90 mAh g^{-1}) under 5 C. We believe that our design here affords a feasible and extended lifespan Li-metal anode with enhanced safety and hastens the development toward next-generation Li-metal batteries.

ASSOCIATED CONTENT

Ⓢ Supporting Information

The Supporting Information is available free of charge at https://pubs.acs.org/doi/10.1021/acsaem.2c00148.

Characterizations; additional figures as mentioned in the text: thermogravimetric analyzer curves; more SEM images; N$_2$ adsorption isotherms with the pore size distribution; Raman spectra; XPS spectra; voltage−areal capacity curve; EIS plots; and compatibility of Ni$_2$P@CNF@Li in carbonate electrolytes (PDF)

■ AUTHOR INFORMATION

Corresponding Authors

Lina Wang − *State Key Laboratory for Modification of Chemical Fibers and Polymer Materials, College of Materials Science and Engineering, Donghua University, Shanghai 201620, China;* ⓞ orcid.org/0000-0002-2211-4661; Email: linawang@dhu.edu.cn

Tianxi Liu − *State Key Laboratory for Modification of Chemical Fibers and Polymer Materials, College of Materials Science and Engineering, Donghua University, Shanghai 201620, China; Key Laboratory of Synthetic and Biological Colloids, Ministry of Education, School of Chemical and Material Engineering, Jiangnan University, Wuxi 214122, China;* Email: txliu@dhu.edu.cn

Authors

Cuimei Fu − *State Key Laboratory for Modification of Chemical Fibers and Polymer Materials, College of Materials Science and Engineering, Donghua University, Shanghai 201620, China*

Wangcong Xu − *State Key Laboratory for Modification of Chemical Fibers and Polymer Materials, College of Materials Science and Engineering, Donghua University, Shanghai 201620, China*

Chengzhou Tao − *State Key Laboratory for Modification of Chemical Fibers and Polymer Materials, College of Materials Science and Engineering, Donghua University, Shanghai 201620, China*

Complete contact information is available at:
https://pubs.acs.org/10.1021/acsaem.2c00148

Author Contributions

The manuscript was written through contributions of all authors. All authors have given approval to the final version of the manuscript.

Notes

The authors declare no competing financial interest.

■ REFERENCES

(1) Goodenough, J. B.; Park, K.-S. The Li-Ion Rechargeable Battery: A Perspective. *J. Am. Chem. Soc.* **2013**, *135*, 1167−1176.

(2) Thackeray, M. M.; Wolverton, C.; Isaacs, E. D. Electrical Energy Storage for Transportation—Approaching the Limits of, and Going Beyond, Lithium-Ion Batteries. *Energy Environ. Sci.* **2012**, *5*, 7854−7863.

(3) Xiao, J.; Li, Q.; Bi, Y.; Cai, M.; Dunn, B.; Glossmann, T.; Liu, J.; Osaka, T.; Sugiura, R.; Wu, B.; Yang, J.; Zhang, J.-G.; Whittingham, M. S. Understanding and Applying Coulombic Efficiency in Lithium Metal Batteries. *Nat. Energy* **2020**, *5*, 561−568.

(4) Cheng, X.-B.; Zhang, R.; Zhao, C.-Z.; Zhang, Q. Toward Safe Lithium Metal Anode in Rechargeable Batteries: A Review. *Chem. Rev.* **2017**, *117*, 10403−10473.

(5) Cheng, X.-B.; Huang, J.-Q.; Zhang, Q. Review—Li metal anode in working lithium-sulfur batteries. *J. Electrochem. Soc.* **2018**, *165*, A6058−A6072.

(6) Hong, H.; Che Mohamad, N. A. R.; Chae, K.; Marques Mota, F.; Kim, D. H. The lithium metal anode in Li−S batteries: challenges and recent progress. *J. Mater. Chem. A* **2021**, *9*, 10012−10038.

(7) Cheng, X.-B.; Yan, C.; Huang, J.-Q.; Li, P.; Zhu, L.; Zhao, L.; Zhang, Y.; Zhu, W.; Yang, S.-T.; Zhang, Q. The gap between long lifespan Li-S coin and pouch cells: The importance of lithium metal anode protection. *Energy Storage Mater.* **2017**, *6*, 18−25.

(8) Feng, Y.; Wang, G.; Ju, J.; Zhao, Y.; Kang, W.; Deng, N.; Cheng, B. Towards high energy density Li−S batteries with high sulfur loading: From key issues to advanced strategies. *Energy Storage Mater.* **2020**, *32*, 320−355.

(9) Yu, Y.; Liu, Y.; Xie, J. Building Better Li Metal Anodes in Liquid Electrolyte: Challenges and Progress. *ACS Appl. Mater. Interfaces* **2021**, *13*, 18−33.

(10) Ramasubramanian, A.; Yurkiv, V.; Foroozan, T.; Ragone, M.; Shahbazian-Yassar, R.; Mashayek, F. Stability of Solid-Electrolyte Interphase (SEI) on the Lithium Metal Surface in Lithium Metal Batteries (LMBs). *ACS Appl. Energy Mater.* **2020**, *3* (11), 10560−10567.

(11) Liu, W.; Liu, P.; Mitlin, D. Tutorial Review on Structure − Dendrite Growth Relations in Metal Battery Anode Supports. *Chem. Soc. Rev.* **2020**, *49*, 7284−7300.

(12) Chen, S.; Dai, F.; Cai, M. Opportunities and Challenges of High-Energy Lithium Metal Batteries for Electric Vehicle Applications. *ACS Energy Lett.* **2020**, *5*, 3140−3151.

(13) Yue, C.; Sun, S.; Jang, M.; Park, E.; Son, B.; Son, H.; Liu, Z.; Wang, D.; Paik, U.; Song, T. A Robust Solid Electrolyte Interphase Layer Coated on Polyethylene Separator Surface Induced by Ge Interlayer for Stable Li-Metal Batteries. *Electrochim. Acta* **2021**, *370*, 137703.

(14) Li, T.; Zhang, X.-Q.; Shi, P.; Zhang, Q. Fluorinated Solid-Electrolyte Interphase in High-Voltage Lithium Metal Batteries. *Joule* **2019**, *3*, 2647−2661.

(15) Westover, A. S.; Dudney, N. J.; Sacci, R. L.; Kalnaus, S. Deposition and Confinement of Li Metal along an Artificial Lipon−Lipon Interface. *ACS Energy Lett.* **2019**, *4*, 651−655.

(16) Trinh, N. D.; Lepage, D.; Aymé-Perrot, D.; Badia, A.; Dollé, M.; Rochefort, D. An Artificial Lithium Protective Layer that Enables the Use of Acetonitrile-Based Electrolytes in Lithium Metal Batteries. *Angew. Chem., Int. Ed.* **2018**, *57*, 5072−5075.

(17) Huang, Y.; Geng, Z.; Sun, G.; Zheng, J.; Li, H. Interfacial Layer Rich in Organic Fluoride Enabling Stable Cycling of High-Voltage PEO-Based Solid-State Lithium Batteries. *Electrochim. Acta* **2022**, *404*, 139617.

(18) Wondimkun, Z. T.; Tegegne, W. A.; Shi-Kai, J.; Huang, C.-J.; Sahalie, N. A.; Weret, M. A.; Hsu, J.-Y.; Hsieh, P.-L.; Huang, Y.-S.; Wu, S.-H.; Su, W.-N.; Hwang, B. J. Highly-Lithiophilic Ag@PDA-GO Film to Suppress Dendrite Formation on Cu Substrate in Anode-Free Lithium Metal Batteries. *Energy Storage Mater.* **2021**, *35*, 334−344.

(19) Meyerson, M. L.; Papa, P. E.; Heller, A.; Mullins, C. B. Recent Developments in Dendrite-Free Lithium-Metal Deposition through Tailoring of Micro- and Nanoscale Artificial Coatings. *ACS Nano* **2021**, *15*, 29−46.

(20) Lin, L.; Liang, F.; Zhang, K.; Mao, H.; Yang, J.; Qian, Y. Lithium Phosphide/Lithium Chloride Coating on Lithium for Advanced Lithium Metal Anode. *J. Mater. Chem. A* **2018**, *6*, 15859−15867.

(21) Wu, C.; Guo, F.; Zhuang, L.; Ai, X.; Zhong, F.; Yang, H.; Qian, J. Mesoporous Silica Reinforced Hybrid Polymer Artificial Layer for High-Energy and Long-Cycling Lithium Metal Batteries. *ACS Energy Lett.* **2020**, 5 (5), 1644−1652.

(22) Chen, K.-H.; Wood, K. N.; Kazyak, E.; LePage, W. S.; Davis, A. L.; Sanchez, A. J.; Dasgupta, N. P. Dead Lithium: Mass Transport

Effects on Voltage, Capacity, and Failure of Lithium Metal Anodes. *J. Mater. Chem. A* **2017**, *5*, 11671−11681.

(23) Park, S.; Jin, H.-J.; Yun, Y. S. Advances in the Design of 3D-Structured Electrode Materials for Lithium-Metal Anodes. *Adv. Mater.* **2020**, *32*, 2002193.

(24) Ke, X.; Liang, Y.; Ou, L.; Liu, H.; Chen, Y.; Wu, W.; Cheng, Y.; Guo, Z.; Lai, Y.; Liu, P.; Shi, Z. Surface Engineering of Commercial Ni Foams for Stable Li Metal Anodes. *Energy Storage Mater.* **2019**, *23*, 547−555.

(25) Liu, W.; Xia, Y.; Wang, W.; Wang, Y.; Jin, J.; Chen, Y.; Paek, E.; Mitlin, D. Pristine or Highly Defective? Understanding the Role of Graphene Structure for Stable Lithium Metal Plating. *Adv. Energy Mater.* **2019**, *9*, 1802918.

(26) Matsuda, S.; Kubo, Y.; Uosaki, K.; Nakanishi, S. Insulative Microfiber 3D Matrix as a Host Material Minimizing Volume Change of the Anode of Li Metal Batteries. *ACS Energy Lett.* **2017**, *2*, 924−929.

(27) Stolz, L.; Homann, G.; Winter, M.; Kasnatscheew, J. The Sand Equation and its Enormous Practical Relevance for Solid-State Lithium Metal Batteries. *Mater. Today* **2021**, *44*, 9−14.

(28) Liu, W.; Lin, D.; Pei, A.; Cui, Y. Stabilizing Lithium Metal Anodes by Uniform Li-Ion Flux Distribution in Nanochannel Confinement. *J. Am. Chem. Soc.* **2016**, *138*, 15443−15450.

(29) Noh, J.; Tan, J.; Yadav, D. R.; Wu, P.; Xie, K. Y.; Yu, C. Understanding of Lithium Insertion into 3D Porous Carbon Scaffolds with Hybridized Lithiophobic and Lithiophilic Surfaces by In-Operando Study. *Nano Lett.* **2020**, *20*, 3681−3687.

(30) Chen, X.; Chen, X.-R.; Hou, T.-Z.; Li, B.-Q.; Cheng, X.-B.; Zhang, R.; Zhang, Q. Lithiophilicity Chemistry of Heteroatom-Doped Carbon to Guide Uniform Lithium Nucleation in Lithium Metal Anodes. *Sci. Adv.* **2019**, *5*, No. eaau7728.

(31) Yan, K.; Lu, Z.; Lee, H.-W.; Xiong, F.; Hsu, P.-C.; Li, Y.; Zhao, J.; Chu, S.; Cui, Y. Selective Deposition and Stable Encapsulation of Lithium through Heterogeneous Seeded Growth. *Nat. Energy* **2016**, *1*, 16010.

(32) Yun, J.; Park, B.-K.; Won, E.-S.; Choi, S. H.; Kang, H. C.; Kim, J. H.; Park, M.-S.; Lee, J.-W. Bottom-Up Lithium Growth Triggered by Interfacial Activity Gradient on Porous Framework for Lithium-Metal Anode. *ACS Energy Lett.* **2020**, *5*, 3108−3114.

(33) Li, Y.-N.; Wang, C.-Y.; Gao, R.-M.; Cao, F.-F.; Ye, H. Recent Smart Lithium Anode Configurations for High-Energy Lithium Metal Batteries. *Energy Storage Mater.* **2021**, *38*, 262−275.

(34) Phattharasupakun, N.; Wutthiprom, J.; Duangdangchote, S.; Sawangphruk, M. A 3D Free-Standing Lithiophilic Silver Nanowire Aerogel for Lithium Metal Batteries without Lithium Dendrites and Volume Expansion: In Operando X-ray Diffraction. *Chem. Commun.* **2019**, *55*, 5689−5692.

(35) Zhuang, H.; Zhao, P.; Li, G.; Xu, Y.; Jia, X. Li−LiAl alloy composite with memory effect as high-performance lithium metal anode. *J. Power Sources* **2020**, *455*, 227977.

(36) Luan, C.; Chen, L.; Li, B.; Zhu, L.; Li, W. Electrochemical Dealloying-Enabled 3D Hierarchical Porous Cu Current Collector of Lithium Metal Anodes for Dendrite Growth Inhibition. *ACS Appl. Energy Mater.* **2021**, *4*, 13903−13911.

(37) Chen, T.; Jianjian, S.; Xing, J.; Liu, Y.; Wang, Z.; Xiao, J.; Liu, H.; Chen, Y.; Sun, X.; Li, J. Self-Formed Lithiophilic Alloy Buffer Layer on Copper Foam Framework for Advanced Lithium Metal Anodes. *ACS Appl. Energy Mater.* **2021**, 4 (5), 4879−4886.

(38) Zhai, P.; Liu, L.; Wei, Y.; Zuo, J.; Yang, Z.; Chen, Q.; Zhao, F.; Zhang, X.; Gong, Y. Self-Healing Nucleation Seeds Induced Long-Term Dendrite-Free Lithium Metal Anode. *Nano Lett.* **2021**, *21*, 7715−7723.

(39) Yu, C.; Du, Y.; He, R.; Ma, Y.; Liu, Z.; Li, X.; Luo, W.; Zhou, L.; Mai, L. Hollow SiO$_x$/C Microspheres with Semigraphitic Carbon Coating as the "Lithium Host" for Dendrite-Free Lithium Metal Anodes. *ACS Appl. Energy Mater.* **2021**, *4*, 3905−3912.

(40) Yue, X.-Y.; Wang, W.-W.; Wang, Q.-C.; Meng, J.-K.; Zhang, Z.-Q.; Wu, X.-J.; Yang, X.-Q.; Zhou, Y.-N. CoO Nanofiber Decorated Nickel Foams as Lithium Dendrite Suppressing Host Skeletons for

High Energy Lithium Metal Batteries. *Energy Storage Mater.* **2018**, *14*, 335−344.

(41) Zhang, R.; Li, Y.; Qiao, L.; Li, D.; Deng, J.; Zhou, J.; Xie, L.; Hou, Y.; Wang, T.; Tian, W.; Cao, J.; Cheng, F.; Yang, B.; Liang, K.; Chen, P.; Kong, B. Atomic Layer Deposition Assisted Superassembly of Ultrathin ZnO Layer Decorated Hierarchical Cu Foam for Stable Lithium Metal Anode. *Energy Storage Mater.* **2021**, *37*, 123−134.

(42) Huang, Z.; Zhang, C.; Lv, W.; Zhou, G.; Zhang, Y.; Deng, Y.; Wu, H.; Kang, F.; Yang, Q.-H. Realizing stable lithium deposition by in situ grown Cu_2S nanowires inside commercial Cu foam for lithium metal anodes. *J. Mater. Chem. A* **2019**, *7*, 727−732.

(43) Loaiza, L. C.; Monconduit, L.; Seznec, V. Si and Ge-Based Anode Materials for Li-, Na-, and K-Ion Batteries: A Perspective from Structure to Electrochemical Mechanism. *Small* **2020**, *16*, 1905260.

(44) Yang, Y.; Zheng, G.; Cui, Y. Nanostructured Sulfur Cathodes. *Chem. Soc. Rev.* **2013**, *42* (7), 3018−3032.

(45) Harada, K.; Hibino, M.; Kobayashi, H.; Ogasawara, Y.; Okuoka, S.-i.; Yonehara, K.; Ono, H.; Sumida, Y.; Yamaguchi, K.; Kudo, T.; Mizuno, N. Electrochemical Reactions and Cathode Properties of Fe-doped Li_2O for the Hermetically Sealed Lithium Peroxide Battery. *J. Power Sources* **2016**, *322*, 49−56.

(46) Sun, C.; Lin, A.; Li, W.; Jin, J.; Sun, Y.; Yang, J.; Wen, Z. In Situ Conversion of Cu_3P Nanowires to Mixed Ion/Electron-Conducting Skeleton for Homogeneous Lithium Deposition. *Adv. Energy Mater.* **2020**, *10*, 1902989.

(47) Luo, Z.; Li, S.; Yang, L.; Tian, Y.; Xu, L.; Zou, G.; Hou, H.; Wei, W.; Chen, L.; Ji, X. Interfacially Redistributed Charge for Robust Lithium Metal Anode. *Nano Energy* **2021**, *87*, 106212.

(48) Nazri, G. Preparation, structure and ionic conductivity of lithium phosphide. *Solid State Ionics* **1989**, *34* (1), 97−102.

(49) Zheng, Y.; Chen, S.; Zhang, K. A. I.; Guan, J.; Yu, X.; Peng, W.; Song, H.; Zhu, J.; Xu, J.; Fan, X.; Zhang, C.; Liu, T. Template-Free Construction of Hollow Mesoporous Carbon Spheres from a Covalent Triazine Framework for Enhanced Oxygen Electro-reduction. *J. Colloid Interface Sci.* **2022**, *608*, 3168−3177.

(50) Zheng, Y.; Song, H.; Chen, S.; Yu, X.; Zhu, J.; Xu, J.; Zhang, K. A. I.; Zhang, C.; Liu, T. Metal-Free Multi-Heteroatom-Doped Carbon Bifunctional Electrocatalysts Derived from a Covalent Triazine Polymer. *Small* **2020**, *16*, 2004342.

(51) Bernasconi, R.; Khalil, M. I.; Iaquinta, C.; Lenardi, C.; Nobili, L.; Magagnin, L. Nickel Phosphides Fabricated through a Codeposition−Annealing Technique as Low-Cost Electrocatalytic Layers for Efficient Hydrogen Evolution Reaction. *ACS Appl. Energy Mater.* **2020**, *3*, 6525−6535.

(52) Jin, Y.; Zhao, C.; Wang, L.; Jiang, Q.; Ji, C.; He, X. Preparation of Mesoporous Ni_2P Nanobelts with High Performance for Electrocatalytic Hydrogen Evolution and Supercapacitor. *Int. J. Hydrogen Energy* **2018**, *43*, 3697−3704.

(53) Ji, L.; Wei, Y.; Wu, P.; Xu, M.; Wang, T.; Wang, S.; Liang, Q.; Meyer, T. J.; Chen, Z. Heterointerface Engineering of $Ni_2P−Co_2P$ Nanoframes for Efficient Water Splitting. *Chem. Mater.* **2021**, *33*, 9165−9173.

(54) Wang, J.; Wang, P.; Hou, J.; Qian, J.; Wang, C.; Ao, Y. In situ Surface Engineering of Ultrafine Ni_2P Nanoparticles on Cadmium Sulfide for Robust Hydrogen Evolution. *Catal. Sci. Technol.* **2018**, *8*, 5406−5415.

(55) Gao, R.; Pan, L.; Wang, H.; Zhang, X.; Wang, L.; Zou, J.-J. Ultradispersed Nickel Phosphide on Phosphorus-Doped Carbon with Tailored d-Band Center for Efficient and Chemoselective Hydro-genation of Nitroarenes. *ACS Catal.* **2018**, *8*, 8420−8429.

(56) Song, T.; Ren, P.; Ma, Z.; Xiao, J.; Yang, Y. Highly Dispersed Single-Phase Ni_2P Nanoparticles on N,P-Codoped Porous Carbon for Efficient Synthesis of N-Heterocycles. *ACS Sustainable Chem. Eng.* **2020**, *8*, 267−277.

(57) Zheng, Y.; Chen, S.; Zhang, K. A. I.; Zhu, J.; Xu, J.; Zhang, C.; Liu, T. Ultrasound-Triggered Assembly of Covalent Triazine Framework for Synthesizing Heteroatom-Doped Carbon Nanoflowers Boosting Metal-Free Bifunctional Electrocatalysis. *ACS Appl. Mater. Interfaces* **2021**, *13*, 13328−13337.

(58) Du, W.; Han, F.; Zhang, M.; Qian, C.; Yang, X. Temperature-Dependent Synthesis of MOF-Derived Co@N-Doped Carbon Nanotube Nanocomposites toward Accelerated Reduction of 4-Nitrophenol. *Compos. Commun.* **2021**, *25*, 100718.

(59) Fu, C.; Yang, H.; Feng, G.; Wang, L.; Liu, T. In-situ Reducing Synthesis of MoP@nitrogen-Doped Carbon Nanofibers as an Anode Material for Lithium/Sodium-Ion Batteries. *Electrochim. Acta* **2020**, *358*, 136921.

(60) Zhang, H.-J.; Cai, C.; Zhang, S.; Ma, Z.-F.; Xue, Y.; Yan, W.; Zhang, J. Metathesis Reaction to Form Nanosheet-Structured $Co(OH)_2$ Deposited on N-Doped Carbon as Composite Electro-catalysts for Oxygen Reduction. *ACS Appl. Energy Mater.* **2021**, *4*, 4165−4172.

(61) Yang, G.; Li, X.; Guan, Z.; Tong, Y.; Xu, B.; Wang, X.; Wang, Z.; Chen, L. Insights into Lithium and Sodium Storage in Porous Carbon. *Nano Lett.* **2020**, *20*, 3836−3843.

(62) Simon, P.; Gogotsi, Y.; Dunn, B. Where Do Batteries End and Supercapacitors Begin? *Science* **2014**, *343*, 1210−1211.

(63) Gogotsi, Y.; Penner, R. M. Energy Storage in Nanomaterials−Capacitive, Pseudocapacitive, or Battery-like? *ACS Nano* **2018**, *12*, 2081−2083.

(64) Krauskopf, T.; Hartmann, H.; Zeier, W. G.; Janek, J. Toward a Fundamental Understanding of the Lithium Metal Anode in Solid-State Batteries—An Electrochemo-Mechanical Study on the Garnet-Type Solid Electrolyte $Li_{6.25}Al_{0.25}La_3Zr_2O_{12}$. *ACS Appl. Mater. Interfaces* **2019**, *11*, 14463−14477.

(65) Li, Y.; Yang, Z.; Wu, Z.; Li, J.; Zou, J.; Jiang, C.; Yang, J.; Wang, L.; Niu, X. The effects of lithium salt and solvent on lithium metal anode performance. *Solid State Ionics* **2018**, *324*, 144−149.

(66) Yang, H.; Guo, C.; Naveed, A.; Lei, J.; Yang, J.; Nuli, Y.; Wang, J. Recent progress and perspective on lithium metal anode protection. *Energy Storage Mater.* **2018**, *14*, 199−221.